HIAPER Cloud Radar (HCR) data (CfRadial), Version 3.1

Changes from Version 3.0

In the Particle IDentification (PID) field a temperature threshold of -40 °C was set. Liquid particles are no longer allowed at temperatures below this threshold and were set to precipitation or cloud.

Overview

This dataset contains HIAPER Cloud Radar (HCR) data collected aboard the NSF/NCAR GV HIAPER (Gulfstream-V High-performance Instrumented Airborne Platform for Environmental Research, HIAPER) (N677F) during OTREC (Organization of Tropical East Pacific Convection). The data were collected during 22 research flights which took place between August 7 and October 2, 2019, over the East Pacific and extreme SW Caribbean Ocean. For more information on OTREC, see https://www.eol.ucar.edu/field_projects/otrec.

Flight	Date	Start time UTC	End time UTC
RF01	2019 08 07	12:15	17:40
RF02	2019 08 11	12:15	18:15
RF03	2019 08 12	12:15	17:40
RF04	2019 08 16	12:15	18:40
RF05	2019 08 17	12:15	18:00
RF06	2019 08 18	13:15	18:45
RF07	2019 08 22	13:15	19:20
RF08	2019 08 23	12:15	17:35
RF09	2019 08 25	12:30	18:55
RF10	2019 09 03	12:10	18:20
RF11	2019 09 04	12:10	17:10
RF12	2019 09 09	14:00	20:25
RF13	2019 09 17	14:25	19:55
RF14	2019 09 21	12:05	18:10
RF15	2019 09 22	12:15	17:55
RF16	2019 09 24	12:05	17:30
RF17	2019 09 25	12:10	17:30
RF18	2019 09 27	12:10	17:40
RF19	2019 09 28	14:15	19:10
RF20	2019 09 30	12:05	17:25

RF21	2019 10 01	12:05	17:45
RF22	2019 10 02	12:05	16:25

Instrument description

HCR is an airborne, polarimetric, millimeter-wavelength (W-band) radar that serves the atmospheric science community by providing cloud remote sensing capabilities to the NSF/NCAR G-V (HIAPER) aircraft. HCR detects drizzle, and ice and liquid clouds, and collects Doppler radial velocity measurements, which at vertical incident include the vertical wind speed and particle fall speed.

In a pod-based design, a single lens antenna is used for both transmit and receive. The transceiver uses a two-stage up and down conversion superheterodyne design. The transmit waveform, from a waveform generator, passes through the two-stage up-conversion to the transmit frequency of 94.40 GHz. It is then amplified by an extended interaction klystron amplifier (EIKA) to 1.6 kW peak power. System performance on transmit and receive paths are closely monitored using a coupler and a noise source. Raw in-phase and quadrature information are archived in HCR. For more information, see Vivekanandan et al. (2015) and www.eol.ucar.edu/instruments/hiaper-cloud-radar-hcr

HIAPER Cloud Radar Specifications	
Parameter	**Specification**
Antenna	0.30 m, lens
Antenna gain	46.21 dB
Antenna 3 dB beam width	0.73°
Transmit Polarization	Linear (V)
Transmit frequency	94.40 GHz
Transmitter	Klystron
Peak transmit power	1.6 kW
Pulse width	0.2 – 1.0 µs
PRF	up to 10 kHz
System noise power	-101 dBm
Receiver noise figure	8.9 dB
Receiver Bandwidth	20 MHz
Receiver Dynamic Range	76 dB
First IF	156.25 MHz

Second IF	1406.25 MHz
Range resolution	20 - 180 m
Unambiguous range	15 km
Typical reflectivity uncertainty	0.4 dB
Sensitivity	-35.0 dBZ at 1 km and 256 ns pulse
Unambiguous velocity	±7.75 m/s
Typical radial velocity uncertainty	0.2 m/s at W=2 m/s
Dwell time	100 ms

Data description

The 10 Hz moments data described here are available at
http://data.eol.ucar.edu/dataset/590.009 in CfRadial format. For more information on CfRadial
see www.ral.ucar.edu/projects/titan/docs/radial_formats/CfRadialDoc.pdf.

The primary data products for scientific use are listed in the table below.

Variable	Dimensions	Unit	Long Name
time	time	seconds	Time in seconds since volume start
	time	meters	Range from instrument to center of gate
latitude	time	deg	Latitude
longitude	time	deg	Longitude
altitude	time	meters	Altitude of radar
DBZ	time, range	dBZ	Reflectivity
DBZ_MASKED	time, range	dBZ	Reflectivity of cloud echo only (DBZ(FLAG>1)=NAN, see FLAG below)
VEL_CORR	time, range	m/s	Motion and bias corrected Doppler velocity
WIDTH	time, range	m/s	Spectral width
SNR	time, range	dB	Signal to noise ratio
DBMVC	time, range	dBm	Log power co-polar v transmit, v receive
DBMHX	time, range	dBm	Log power cross-polar v transmit, h receive
NCP	time, range		Normalized coherent power
LDR	time, range	dB	Linear depolarization ratio (V/H)
PRESS	time, range	hPa	Air pressure from ERA5

TEMP	time, range	C	Air temperature from ERA5
RH	time, range	%	Relative humidity from ERA5
SST	time	C	Sea surface temperature from ERA5 forecast
U_SURF	time	m/s	Surface U wind component from ERA5 forecast
V_SURF	time	m/s	Surface V wind component from ERA5 forecast
TOPO	time	m	Terrain elevation above mean sea level from GTOPO30 (U.S. Geological Survey, 2019)
FLAG	time, range		See Romatschke et al. (2021) Flag field to classify reflectivity (to mask unwanted data): 1 Cloud 2 Speckle (contiguous 2D echo areas of < 100 pixels) 3 Extinct (signal completely attenuated) 4 Backlobe echo (reflection from the land/sea surface when zenith pointing and flying low) 5 Out of range (second trip echo from land/sea surface when flying too high) 6 Transmitter pulse (echo from within the radar itself) 7 Water surface echo 8 Land surface echo 9 Below the surface 10 Noise source calibration 11 Antenna in transition (e.g. from nadir to zenith or vice versa) 12 Missing (not transmitting)
ANTFLAG	time		Flag field to indicate the status of the antenna: 0 Down (nadir pointing) 1 Up (zenith pointing) 2 Pointing (pointing to an angle different from nadir or zenith) 3 Scanning (e.g. sea surface calibration) 4 Transition (e.g. from nadir to zenith)
MELTING_LAYER	time, range		See Romatschke (2021) 10 below icing level 11 ERA5 0 °C isotherm below icing level 12 detected melting layer below or at icing level 13 interpolated melting layer below or at icing level 14 estimated melting layer below or at icing level 20 above icing level 21 ERA5 0 °C isotherm above icing level 22 detected melting layer above icing level 23 interpolated melting layer above icing level 24 estimated melting layer above icing level
ICING_LEVEL	time		Icing level, which is defined as the lowest melting layer
ECHO_TYPE_2D	time, range		See Romatschke and Dixon (2022)

			14 stratiform low 16 stratiform mid 18 stratiform high 25 mixed 30 convective 32 convective elevated 34 convective shallow 36 convective mid 38 convective deep
ECHO_TYPE_1D	time		As ECHO_TYPE_2D
PID	time, range		See Romatschke and Vivekanandan (2022) 1 rain 2 supercooled rain 3 drizzle 4 supercooled drizzle 5 cloud liquid 6 supercooled cloud liquid 7 melting 8 large frozen 9 small frozen 10 precipitation 11 cloud

Data processing and quality control

A detailed description of the data processing and quality control procedures can be found in Romatschke et al. (2021).

Noise source calibration and temperature dependency correction

As an external, pod-mounted system, which is deployed in a wide range of altitudes from near surface to approximately 47,000 feet, HCR experiences large temperature variations. To maintain good system calibration, it is essential to monitor the radar system performance versus temperature. In order to ensure operational accuracy, a number of noise source calibration (NSC) events were performed during OTREC research flights, and on the ground. During each NSC event, a known noise signal, which is invariant to temperature changes, is injected into the radar and then used to characterize the receiver gain changes by comparing the received power (DBMVC) to a temperature-corrected noise power.

As the low noise amplifiers (LNAs) dictate the receiver's performance, they are outfitted with heater circuits to maintain their temperatures between 37^0 and 40^0 C in the bench test

environment. During deployment, as the heaters cycle on and off, the received power level (DBMVC) directly correlates to the temperature fluctuations, leading to a sinusoidal pattern which cycles around 34^0 C when installed in the system. In some extreme cases, after flying at ~47,000 ft for several hours, the heaters of the LNAs could not keep up with the heat loss to the environment, leading to a significant decline of the received power. Using the correlation between the LNA temperature and the received power level during the NSC events we calculated the correlation equation which we used (together with the calibration data obtained in the lab) to correct the power fields (DBMVC, DBMHX, and DBZ) for LNA temperature changes in the whole data set.

As mentioned above, the received power not only depends on the LNA temperatures but also on the pod temperature. After correcting for the LNA temperature changes we were able to establish a correlation between the pod temperature and the power output during the NSC events which was then again used to correct the whole data set. (Note that we define a mean of the Noise Source, EIK, Polarization Switch, and RF Detector temperatures as the "pod temperature".)

Sea surface calibration check

Based on the work of Li et al. (2005) we use the backscattering properties of the ocean surface to assess how well HCR reflectivity is calibrated. Over 40 sea surface calibration (SSC) events were performed during OTREC, each consisting of a few minutes of cross-track scanning from 20° to -20° off-nadir. Again following Li et al. (2005) we used

$$\sigma_{0meas} = dBZ + 10log_{10}\left(\frac{\pi^5 c\tau\,|K|^2}{2\lambda^4 10^{18}}\right) + 2l_{a0} - 10log_{10}\left(cos\Theta\right)$$

to calculate the normalized radar cross section $\sigma_{0\ meas}$ of HCR in dB, where Z is the measured reflectivity, c is the speed of light m s^{-1}, τ is the pulse width s, $|K|^2$ is the radar dielectric factor, λ is the signal wavelength in m, l_{a0} is the nadir atmospheric attenuation in dB, and Θ is the elevation angle in degrees.

The measured $\sigma_{0\ meas}$ is then compared to theoretical values of the normalized ocean surface radar cross section $\sigma_{0\ theory}$ which were obtained from three models by Cox and Munk (1954), Freilich and Vanhoff (2003), and Wu (1972, 1990). $\sigma_{0\ theory}$ depends on the surface wind speed, and the sea surface temperature (SST). A weak dependency on ocean salinity is ignored. The wind speed and SST are obtained by 4D interpolation of ERA5 data onto the HCR time x range grid.

The atmospheric attenuation was calculated using the methods of Liebe (1985) and the ITU Recommendation (2013). Both methods depend on atmospheric pressure, temperature, and relative humidity which are again obtained from ERA5 data. The attenuation results of the two methods differed by ~0.2 dB.

Comparison of $\sigma_{0\,meas}$ and $\sigma_{0\,theory}$ reveals a bias of $\sigma_{0\,meas}$ - $\sigma_{0\,theory}$ = ~1-2 dB depending on the model and the specific SSC event. That means that the HCR reflectivity data is likely biased high by between 1 and 2 dB.

Velocity correction

The radial velocity is corrected for platform motion using two different methods. The first corrects for platform motion using INS/GPS measurements. It is applied to all of the data. An additional correction is applied to the nadir-looking data only: The radial velocity of the surface, which is assumed to be 0 m/s, is used as a reference to correct the data with a running 3rd degree polynomial filter of length 15 seconds (Ellis et al., 2019).

Width correction

The radar has a 0.73 degree beam width. Therefore, when pointing nadir or zenith, the beam spread is about 0.36 degrees forward of vertical, and 0.36 degrees aft of the vertical. The sine of 0.36 degrees is 0.006, so at a ground speed of 200 m/s the velocity error at the forward edge of the beam is -0.006 x 200 = -1.2 m/s, since the motion is towards the radar. Similarly the velocity error at the aft edge of the beam is +1.2 m/s. These errors, across the width of the beam, increases the variance of the measured velocity, and hence increase the spectrum width. The computed width correction (delta below) is based on ground speed and beam width, and attempts to correct for this increase.

$$\delta = |(0.3 * speed * sin(elevation) * beamWidthRadians)|$$
$$corrected = \sqrt{(measured^2 - \delta^2)}$$

Known problems

Multiple scattering

In areas of heavy convection HCR data is affected by multiple scattering. Affected areas show increased LDR as seen in the example below. Reflectivity in these areas is likely not accurate and should be used with caution. PID is likely also not accurate. We are currently investigating the multiple scattering problem and hope to have more information in the future.
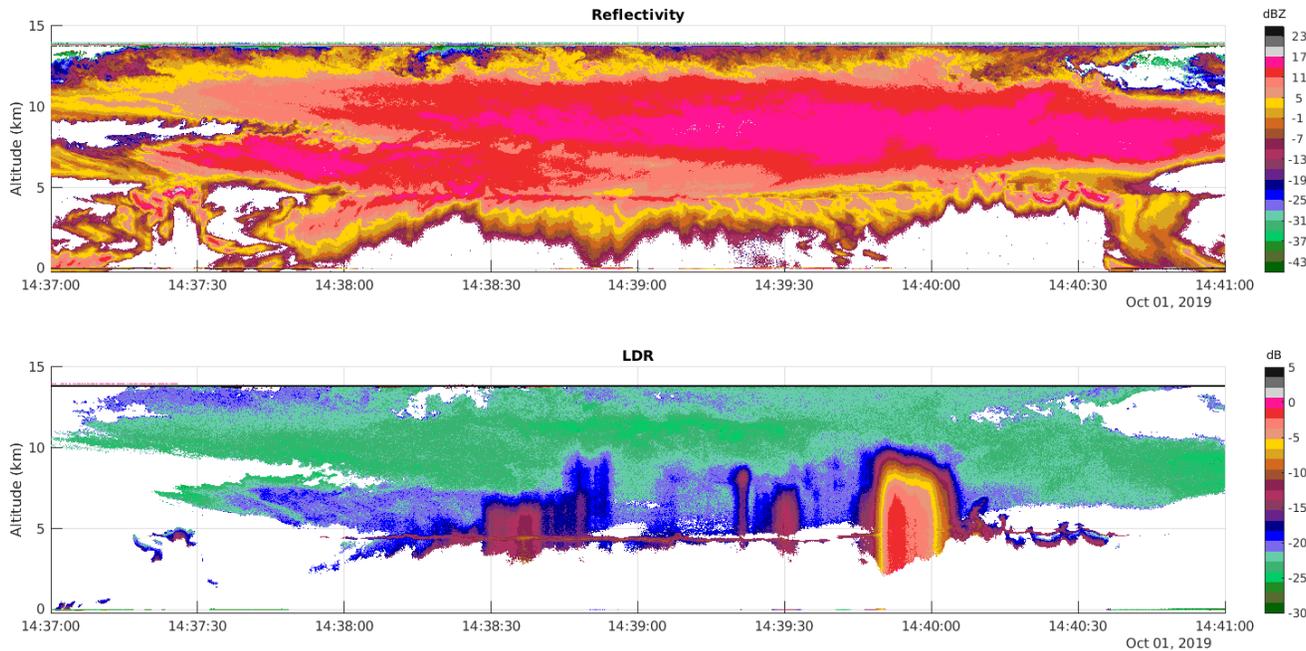
Radial velocity

The surface based velocity correction worked well the majority of the time, however there are some regions in which problems were noted. These problems manifest themselves as columns of biased radial velocity at each range bin over several rays. We think these velocity pillars are caused by the filtering process over-smoothing surface velocity variations due to variable pointing error (Ellis et al. 2019).

Another problem that cannot be corrected is, that the radar, while it rotates 360˚ around the along-plane axis, has only limited range of motion along the cross-plane axis. This means, that when the plane has significant pitch, e.g. during steep climbs, the tilt angle correction of the radar is not sufficient, reports erroneous angles, and the first step of the velocity correction fails. In nadir pointing mode, this can partly be compensated with the second correction step but in zenith pointing mode the velocities are unreliable in these situations.

Backlobe echo in zenith pointing

When the HCR is pointing at zenith and the GV is near the surface, there is often an echo that results from the backlobe of the radar reflecting off of the surface. This backlobe contamination is typically characterized by a band of low reflectivity, highly variable radial velocity, and high spectrum width. The backlobe appears in the zenith data at a range equal to the altitude of the radar. So as the GV ascends or descends the backlobe contamination will recede and approach in range, respectively. An attempt was made to identify the backlobe echo and flag it in the FLAG field but the identification process does not always completely remove all backlobe echo as seen in the example below.

Reflectivity (all data)

Flag field

Reflectivity (cloud only, i.e. DBZ(FLAG>1)=NAN)
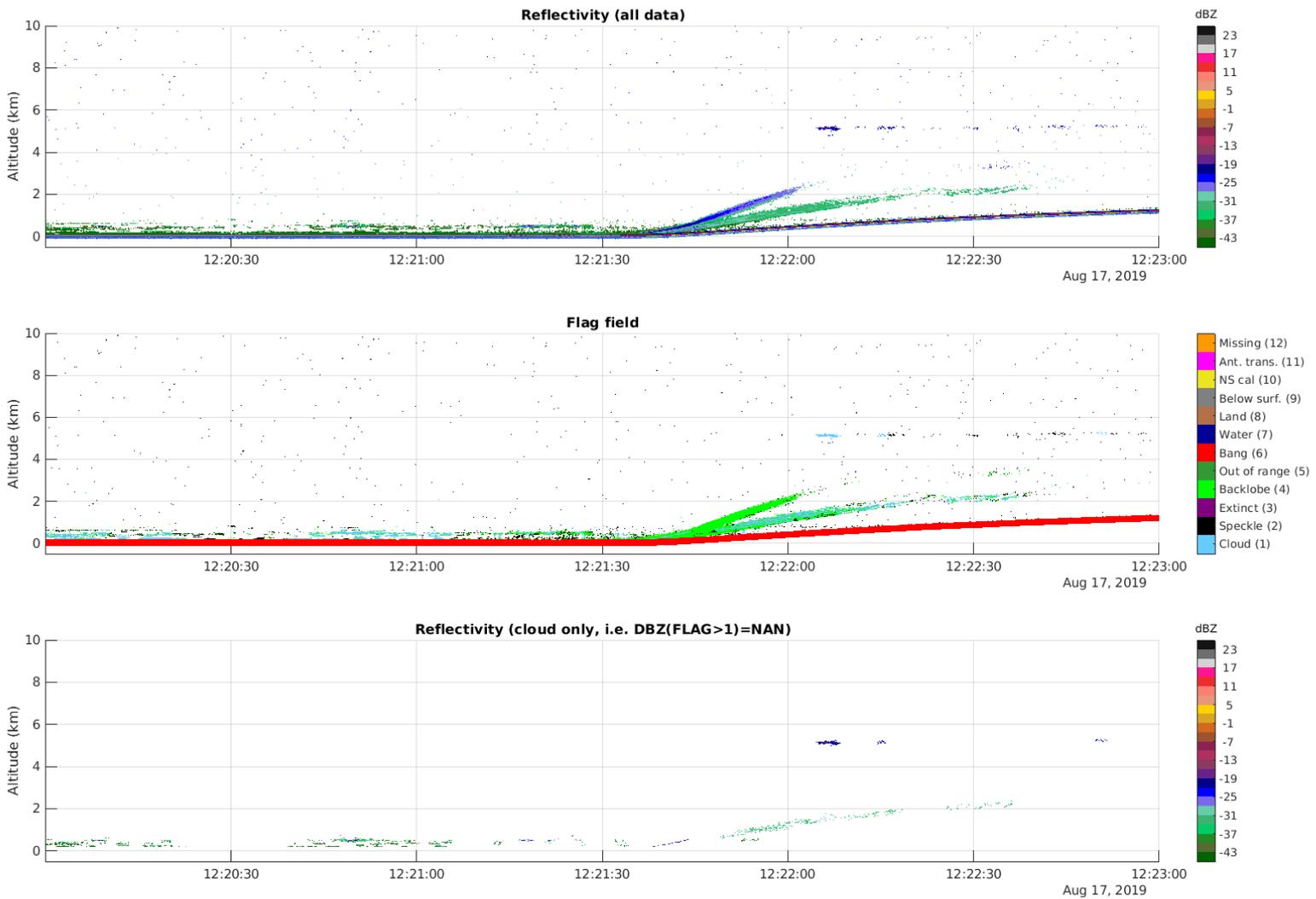
Periods during which the HCR transmitter was disabled

In the HCR data, there are some short periods during which the transmitter was disabled for safety reasons. These show up as gaps in the power fields.

References

Cox, C., and W. Munk, 1954: Measurements of the roughness of the sea surface from photographs of the sun's glitter. J. Opt. Soc. Amer., 144, 838–850.

Ellis, S.M., P. Tsai, C. Burghart, U. Romatschke, M. Dixon, J. Vivekanandan, J. Emmett, and E. Loew, 2019: Use of the Earth's Surface as a Reference to Correct Airborne Nadir-Looking

Radar Radial Velocity Measurements for Platform Motion. J. Atmos. Oceanic Technol., 36, 1343–1360, https://doi-org.cuucar.idm.oclc.org/10.1175/JTECH-D-19-0019.1

European Centre for Medium-Range Weather Forecasts, 2020: ERA5 Reanalysis (0.25 Degree Latitude-Longitude Grid). Research Data Archive at the National Center for Atmospheric Research, Computational and Information Systems Laboratory. doi:10.5065/BH6N-5N20. Accessed January 21, 2020, updated monthly.

Freilich, M. H., and B. A. Vanhoff, 2003: The relationship between winds, surface roughness, and radar backscatter at low incidence angles from TRMM precipitation radar measurements. J. Atmos. Oceanic Technol., 20, 549–562.

ITU Recommendation, 2013: Attenuation by atmospheric gases. Rec. ITU-R P.676-10, 09/2013

Lee, W.-C., P. Dodge, F. D. Marks, and P. H. Hildebrand, 1994: Mapping of airborne Doppler radar data. *J. Atmos. Oceanic Technol*., 11, 572–578.

Li, L., G. M. Heymsfield, L. Tian, and P. E. Racette, 2005: Measurements of Ocean Surface Backscattering Using an Airborne 94-GHz Cloud Radar—Implication for Calibration of Airborne and Spaceborne W-Band Radars. J. Atmos. Oceanic Technol., 22, 1033-1045.

Liebe, H.J., 1985: An updated model for millimeter wave propagation in moist air. Radio Sci., 20, 1069-1089, doi: 10.1029/RS020i005p01069

Romatschke, U: Melting layer detection and observation with the NCAR airborne W-band radar. Remote Sens. 2021.

Romatschke, U.; Dixon, M.; Tsai, P.; Loew, E.; Vivekanandan, J.; Emmett, J.; Rilling, R: 2021: The NCAR Airborne 94-GHz Cloud Radar: Calibration and Data Processing. EarthArXiv, doi:10.31223/X55894.

Romatschke, U., Vivekanandan, V., 2022: Cloud and Precipitation Particle Identification Using Cloud Radar and Lidar Measurements: Retrieval Technique and Validation. Earth and Space Science, 9, e2022EA002299. https://doi.org/10.1029/2022EA002299.

Romatschke, U., Dixon, M., 2022: Vertically Resolved Convective/StratiformEcho Type Identification and ConvectivityRetrieval for Vertically Pointing Radars. EarthArXiv, https://doi.org/10.31223/X54S77.

U.S. Geological Survey, 2019: Global 30 Arc-Second Elevation (GTOPO30). USGS EROS Archive. doi:10.5066/F7DF6PQS.

Vivekanandan, J., Ellis, S., Tsai, P., Loew, E., Lee, W.-C., Emmett, J., Dixon, M., Burghart, C., and Rauenbuehler, S., 2015: A wing pod-based millimeter wavelength airborne cloud radar, Geosci. Instrum. Method. Data Syst., 4, 161-176, https://doi.org/10.5194/gi-4-161-2015

Wu, J., 1972: Sea-surface slope and equilibrium wind–wave spectra. Phys. Fluids, 15, 741–747.

Wu, J., 1990: Mean square slopes of the wind disturbed water surface, their magnitude, directionality, and composition. Radio Sci., 25, 37–48.

Citation

Contact